JOURNAL OF PROPULSION AND POWER
Vol. 9, No. 5, Sept.–Oct. 1993

Unified Navier-Stokes Flowfield and Performance Analysis of Liquid Rocket Engines

Ten-See Wang*
NASA Marshall Space Flight Center, Huntsville, Alabama 35812
and
Yen-Sen Chen†
Engineering Sciences, Inc., Huntsville, Alabama 35805

In an effort to improve the current composite solutions in the design and analysis of liquid propulsive engines, a computational fluid dynamics (CFD) model capable of calculating the reacting flows from the combustion chamber, through the nozzle to the external plume, is developed. Flowfields of a conical nozzle and the Space Shuttle main engine (SSME) fired at sea level are investigated. The CFD model, FDNS (finite difference Navier-Stokes), is a pressure-based, viscous, ideal gas/real gas, reactive flow code. An equilibrium chemistry algorithm is employed using the point implicit method. A conical nozzle with the same expansion ratio as the SSME nozzle is computed to study the shock formation in both the internal and external flowfields. The bell-shaped SSME nozzle is run at 100% power level at various flow conditions. The computed flow solutions and nozzle thrust performance are in good agreement with those of other standard codes and engine hot fire test data.

Nomenclature

A_i = chemical symbol of the ith species
C_{pn} = heat capacity for species n
C_μ = turbulence modeling constant, 0.09
C_v = element molar concentrations
C_1 = turbulence modeling constant, 1.15
C_2 = turbulence modeling constant, 1.9
C_3 = turbulence modeling constant, 0.25
c = local speed of sound
c_i = species molar concentrations
D_i = dissipation terms
d_{iv} = number of element in a species
F = convection and diffusion fluxes
G = geometrical matrices
h = enthalpy
J = Jacobian of coordinate transformation
J_n = diffusion fluxes for species n
K_s = equilibrium constant for sth reaction
k = turbulent kinetic energy
M = total number of elements
M_E = exit Mach number
N = total number of species
Pr = turbulent kinetic energy production
P_{TCE} = total pressure at centerline exit
P_{TWE} = total pressure at wall exit
p = static pressure
q = represents 1, u, v, h, k, ε, and ρ_i
R = gas constant
S_q = source term for equation q
s = local grid cell flow area
T = static temperature
U = transformed velocity
u, v = mean velocities in x and y directions
W_n = mass production rate for species n
x, y = physical coordinates
α_n = mass fraction for species n
β = pressure relaxation parameter
γ = specific heat capacity ratio
ε = turbulent kinetic energy dissipation rate
$\varepsilon_1, \varepsilon_2$ = dissipation parameters
λ = convective dissipation parameter
μ = effective viscosity
μ_l = molecular viscosity
μ_t = turbulent eddy viscosity
ν = artificial dissipation parameter
ξ = computational coordinates
ρ = density
σ_q = turbulence modeling constants
Φ = energy dissipation function

Superscripts
a_{is}, b_{is} = stoichiometric coefficients
n = time level
$'$ = perturbation

Introduction

A SERIES of procedures[1–4] to determine the liquid rocket engine thrust chamber performance and plume flowfield have been developed by governmental and industrial organizations in the mid-sixties. Although improvements to the codes have been made, there are still limitations. The calculation is usually achieved by assembling composite solutions in series. For example, the entire combustion chamber is represented by a point chemical equilibrium analysis, the supersonic flow or the core flow region is solved by the inviscid method of characteristics (MOC) analysis, and the wall and shear layers are described by a separate analysis. The wall layer analysis is restricted to a thin boundary layer, flow separation cannot be predicted, and only axisymmetric flow and steady-state phenomenon can be described.

Accurate numerical prediction of the thrust performance and nozzle/plume flowfield can be achieved with recent ad-

Presented as Paper 90-2494 at the AIAA/ASME/SAE/ASEE 26th Joint Propulsion Conference, Orlando, FL, July 16–18, 1990; received March 30, 1992; revision received Nov. 3, 1992; accepted for publication April 5, 1993. Copyright © 1993 by the American Institute of Aeronautics and Astronautics, Inc. No copyright is asserted in the United States under Title 17, U.S. Code. The U.S. Government has a royalty-free license to exercise all rights under the copyright claimed herein for Governmental purposes. All other rights are reserved by the copyright owner.

*Team Leader, Computational Fluid Dynamics Branch. Member AIAA.
†Senior Staff Scientist. Member AIAA.

vancements in CFD technology without aforementioned limitations. Transient flow can be simulated,[5] and flow reversal has been predicted.[6] Furthermore, advanced CFD technology has three-dimensional capability with applications to dual throat engines, scarfed, integrated nozzles, and cluster nozzles. In Ref. 7, a density-based code PARCH has been applied to a variety of rocket and scramjet propulsive flowfields, albeit no comparison with measurement was made. Reference 8 has used another density-based code RPLUS to calculate the performance and flow for the thrust chamber of a small scale thruster, while performance data was compared. In this study, a pressure-based CFD model is developed for the first time to calculate a unified liquid rocket engine flowfield which describes the main combustion chamber, nozzle, and plume regions simultaneously. Full-scale hot-firing test data on performance and wall pressure were collected and compared. Code validation was achieved by systematically comparing the computational results of the thrust performance and flowfields to those of various industrial codes and hot fire experiments.

Governing Equations

The basic equations employed in this study to describe a unified liquid rocket engine flowfield are the general-coordinate, multicomponent transport equations. The classification of the governing equations changes from one point to another in the unified flowfield. That is, mixed parabolic-hyperbolic type for subsonic chamber flow, and mainly hyperbolic for supersonic nozzle flow. A generalized form of these equations written in curvilinear coordinates is given by

$$\left(\frac{1}{J}\right)\left(\frac{\partial \rho q}{\partial t}\right) = \frac{\partial\left[-\rho U_i q + \mu G_{ij}\left(\frac{\partial q}{\partial \xi_j}\right)\right]}{\partial \xi_i} + \left(\frac{1}{J}\right) S_q$$

where J, U_i, and G_{ij} are written as

$$J = \frac{\partial(\xi, \eta)}{\partial(x, y)}$$

$$U_i = \left(\frac{u_j}{J}\right)\left(\frac{\partial \xi_i}{\partial x_j}\right)$$

$$G_{ij} = \left(\frac{1}{J}\right)\left(\frac{\partial \xi_i}{\partial x_k}\right)\left(\frac{\partial \xi_j}{\partial x_k}\right)$$

$\mu = (\mu_l + \mu_t)/\sigma_q$ is the effective viscosity when the turbulent eddy viscosity concept is employed to model the turbulent flows. $\mu_t = \rho C_\mu k^2/\varepsilon$, is the turbulence eddy viscosity. σ_q and S_q are given in Table 1. $\sigma_h = 0.95$ is the turbulent Prandtl number that is widely used for nozzle flows. An extended two-equation k-ε turbulence model[9] is used to describe the turbulence, while σ_k and σ_ε are taken from that model closure.

The equation of state for an ideal gas is employed for the closure of the above system of equations. A four-step reversible hydrogen/oxygen equilibrium chemistry model is used to close the chemistry system.

Table 1 σ_q and S_q of the transport equations

q	σ_q	S_q
1	1.00	0
u	1.00	$-p_x + \nabla[\mu(u_j)_x] - \frac{2}{3}(\mu \nabla u_j)_x$
v	1.00	$-p_y + \nabla[\mu(u_j)_y] - \frac{2}{3}(\mu \nabla u_j)_y$
h	0.95	$Dp/Dt + \Phi + \Sigma J_n C_{pn} \nabla T - \Sigma h_n W_n$
k	0.89	$\rho(p_r - \varepsilon)$
ε	1.15	$\rho(\varepsilon/k)(C_1 P_r - C_2\varepsilon + C_3 Pr^2/\varepsilon)$
α_n	1.00	$W_n, \quad n = 1, \ldots, N$

Numerical Schemes

An adaptive dissipation scheme was employed to approximate the convective terms of the momentum, energy, and continuity equations; the scheme is based on second- and fourth-order central differencing with artificial dissipation. First-order upwind scheme is used for the species and turbulence equations, since the parameters involved must have positive quantities. Different eigenvalues are used for weighing the dissipation terms depending on the conserved quantity being evaluated, in order to give correct diffusion fluxes near wall boundaries. This procedure is different from those proposed in other works[10-12] in which the sum of the absolute value of the convection velocity and the local speed of sound is used to weigh the dissipation terms. Adding the dissipation term to the convective fluxes F in ξ produces

$$\frac{\partial F}{\partial \xi} \simeq \frac{(F_{i+1} - F_{i-1})}{2} - (D_{i+1/2} - D_{i-1/2})$$

The dissipation terms are constructed such that a fourth-order central and fourth-order damping scheme is activated in smooth regions, and a second-order central and second-order damping scheme is used near shock waves. Since the Jacobian matrices of the Euler fluxes have eigenvalues of U, $U + c$, and $U - c$, it may be sufficient to use the magnitudes of these eigenvalues to weigh the dissipation terms. $U - c$ is not desirable, however, due to the possibility of U changing signs. To maintain the smoothness of the solution with improved accuracy, $|U| + c$ was used for the continuity equation and the minimum damping $|U|$ was used for other transport equations in this study. General forms of the dissipation terms are given for the continuity equation by

$$D_{i+1/2} = D_1(\rho_{i+1} - \rho_i) + D_2(\rho_{i-1} - 3\rho_i + 3\rho_{i+1} - \rho_{i+2})$$

and for other transport equations

$$D_{i+1/2} = D_3(q_{i+1} - q_i) + D_4(q_{i-1} - 3q_i + 3q_{i+1} - q_{i+2}) + (1 - \varepsilon_1)(\rho U_{i+1/2}/16)[(q_i - q_{i-1}) - (q_{i+2} - q_{i+1})]$$

where

$$\begin{aligned}
D_1 &= 0.25\nu_{i+1/2}(|U| + c)_{i+1/2} \\
D_2 &= \max\{0, 0.01 - 0.25\nu_{i+1/2}\}(|U| + c)_{i+1/2} \\
D_3 &= 0.5\varepsilon_1 |\rho U|_{i+1/2} \\
D_4 &= \varepsilon_2(1 - \varepsilon_1)\max\{0.01 s\rho(|u| + |v|), 2|\rho U|\}_{i+1/2} \\
\varepsilon_1 &= \max\{\lambda, \min(1.0, 25\nu_{i+1/2})\} \\
\varepsilon_2 &= 0.015 \\
\nu_{i+1/2} &= \max\{a_i, a_{i+1}\} \\
a_i &= |p_{i+1} - 2p_i + p_{i-1}|/(p_{i+1} + 2p_i + p_{i-1})
\end{aligned}$$

In the above formulations, the values of a_i and $\nu_{i+1/2}$ approach zeros in smooth regions and reach unities near high pressure gradients. For the continuity equation, second-order damping dominates when $\nu_{i+1/2}$ approaches unity and fourth-order damping dominates when $\nu_{i+1/2}$ approaches zero. This is the basis of the adaptive dissipation scheme. For the energy and momentum equations, and in addition to the adaptive dissipation scheme, a parameter λ can be specified to further direct the upwindness, depending on the physics of the flow. An unity λ corresponds to a full upwind scheme, and a vanishing λ corresponds to a central difference scheme in smooth regions. λ is unity for the turbulence and species equations; this is to prevent any cosmetic blemishes near regions of large gradients for the scalar quantities.

A pressure-based solution method was selected so that a wide range of flow speeds could be analyzed with the same code. Successful results of viscous flow computations using pressure-based methods have been reported.[13,14] For high-

speed flow cases, a hyperbolic pressure correction equation was employed by perturbing the density in the mass conservation equation. This provides a smooth transition from low- to high-speed flow characteristics. For time accuracy, a time-centered, time-marching scheme with a multiple pressure correctors algorithm was employed. In general, a noniterative time-marching scheme was used for time-dependent flow computations[5]; however, subiterations can be used if necessary. The multicorrector procedure is described below.

A simplified momentum equation was combined with the continuity equation to form a pressure correction equation. The simplified momentum equation can be written as

$$\frac{\partial \rho u_i}{\partial t} \simeq -\nabla p'$$

or, in discrete form

$$u_i' \simeq -\beta(\Delta t/\rho)\nabla p' \tag{1}$$

The velocity and density fields in the continuity equation for time level $n + 1$ are then perturbed to form a correction equation. That is

$$\left[\frac{\partial \rho}{\nabla t} + \nabla(\rho u_i)\right]^{n+1} = \frac{\partial(\rho^n + \rho')}{\partial t} + \nabla[(\rho^n + \rho')(u_i^n + u_i')] = 0$$

By neglecting the $\rho' u'$ terms, the following equation results:

$$\frac{\partial \rho'}{\partial t} + \nabla(u_i \rho') + \nabla(\rho u_i') = -\left[\frac{\partial \rho}{\partial t} + \nabla(\rho u_i)\right]^n \tag{2}$$

Substituting Eq. (1) into Eq. (2) and letting $\rho' = p'/RT$, the following pressure correction equation is obtained:

$$\frac{\partial(p'/RT)}{\partial t} + \nabla[(u_i/RT)p'] - \nabla(\beta \Delta t \nabla p') = -\left[\frac{\partial \rho}{\partial t} + \nabla(\rho u_i)\right]^n \tag{3}$$

To provide smooth shock solutions the adaptive dissipation terms described above are added to the right side of Eq. (3). Once Eq. (3) is satisfied, the velocity field and the pressure field are updated through Eq. (1) and the following relation:

$$p^{n+1} = p^n + p'$$

The density field is then updated by applying the equation of state. To ensure that the updated velocity, density, and pressure fields satisfy the continuity equation, the above pressure correction solution procedure is repeated several times before marching to the next time step. This represents a multicorrector solution procedure.

The chemistry source terms were evaluated with a point implicit procedure before the species equations were solved. The equilibrium chemistry source terms were based on the CHMQGM algorithm.[15]

Equilibrium Chemistry Algorithm

The chemistry source terms must be computed for each grid point at each time step. The point implicit procedure allows the equilibrium calculation for each grid point to be independent from that of its neighbors and may be treated in isolation. Since kinetics loss was estimated to be negligible in the SSME thrust chamber and nozzle,[16] equilibrium is assumed to exist for the entire computational domain, including the exhaust plume region.

In general, if there are N distinct chemical species composed of M chemical elements, then the algebraic system to be solved consists of N-M nonlinear equilibrium equations and M linear element-conservation relations. The equilibrium reactions are of the form

$$\sum_{i=1}^{N} a_{is} A_i = \sum_{i=1}^{N} b_{is} A_i \qquad s = 1, \ldots, N\text{-}M$$

The equilibrium reactions lead to algebraic relations of the form

$$K_s \prod_{i=1}^{N} [c_i]^{a_{is}} = \prod_{i=1}^{N} [c_i]^{b_{is}} \qquad s = 1, \ldots, N\text{-}M \tag{4}$$

The linear element-conservation reactions are of the form

$$\sum_{i=1}^{N} d_{im} c_i = c_m \qquad m = 1, \ldots, M \tag{5}$$

CHMQGM algorithm has shown that a reduced system can be obtained by substituting the M linear relations, Eq. (5), into the N-M nonlinear relations, Eq. (4). As a result, an iterative Newton-Raphson technique was used to solve a system of N-$2M$ equations rather than the larger equivalent $N \times N$ system. The equilibrium constant approach of CHMQGM is not as general as a minimization of Gibb's free energy approach[17] for an arbitrarily chosen chemical system. However, for a generally well-known hydrogen/oxygen system such as the one being used in SSME, the equilibrium constant approach appears to be more efficient.

Hydrogen/Oxygen Equilibrium Chemistry

The hydrogen/oxygen equilibrium reactions used in this study are a subset reduced from the hydrocarbon combustion partial equilibrium system.[15] It consists of six species (Table 2) and four reactions [Eqs. (6–9) as shown in Table 3].

The element-conservation equations are

$$C_0 = c_1 + c_3 + c_4 + 2c_6 \tag{10}$$

$$C_H = 2c_1 + c_2 + c_4 + 2c_5 \tag{11}$$

Substitute Eqs. (6) and (7) into Eqs. (8) and (9), we have

$$c_6 = R_1(c_3)^2 \qquad R_1 = 1/K_1 \tag{12}$$

$$c_5 = R_2(c_2)^2 \qquad R_2 = 1/K_2 \tag{13}$$

$$c_4 = R_3 c_2 c_3 \qquad R_3 = 1/(K_1 K_2 K_3)^{1/2} \tag{14}$$

$$c_1 = R_4 c_5 c_3 \qquad R_4 = 1/(K_1 K_4)^{1/2} \tag{15}$$

Table 2 Species and reactions considered

Subscript	Species	
1	H_2O	Water vapor
2	H	Atomic hydrogen
3	O	Atomic oxygen
4	OH	Hydroxyl radical
5	H_2	Molecular hydrogen
6	O_2	Molecular oxygen

Table 3 Reactions and equilibrium equations

Reactions	Equilibrium equations	
$O_2 = 2O$	$K_1 c_6 = (c_3)^2$	(6)
$H_2 = 2H$	$K_2 c_5 = (c_2)^2$	(7)
$2OH = O_2 + H_2$	$K_3 (c_4)^2 = c_6 c_5$	(8)
$2H_2O = 2H_2 + O_2$	$K_4 (c_1)^2 = (c_5)^2 c_6$	(9)

Substitute the linear term in Eqs. (12–15) into the linear element-conservation Eqs. (10) and (11), yielding two nonlinear equations and three unknowns in c_2, c_3, and c_5:

$$C_0 = R_4c_5c_3 + c_3 + R_3c_2c_3 + 2R_1(c_3)^2 \quad (16)$$

$$C_H = 2R_4c_5c_3 + c_2 + R_3c_2c_3 + 2R_2(c_2)^2 \quad (17)$$

The final reduced equations can then be obtained by substituting Eq. (16) into Eq. (17), and to eliminate c_5 with Eq. (13), we have

$$R_2R_4(c_2)^2c_3 + R_3c_2c_3 + 2R_1(c_3)^2 + c_3 - C_0 = 0$$

$$R_3c_2c_3 + 4R_1(c_3)^2 + 2c_3 - 2R_2(c_2)^2 - c_2 + (C_H - 2C_0) = 0$$

This reduced system consists of one cubic equation and one quadratic equation with two unknowns, and can readily be solved by Newton-Raphson's iterative method.

Boundary Conditions

Fixed chamber total conditions were used at the inlet of the combustion chamber. Subsonic boundary conditions were used at the inlet of the external ambient air and the pressure was extrapolated. This is to allow the transient disturbances sent from downstream to permeate through the boundary. Flow properties at the wall, centerline and exit were extrapolated from those of the interior domain. To obtain a unique solution for the sea level SSME hot firing sample case, a fixed pressure was applied to the outermost point of the ambient exit boundary.

Sample Cases for SSME at 100% Power Level

SSME operating conditions at 100% power level were used for the calculations. The actual values used are shown in Table 4.

Results of the Inviscid, Ideal Gas, Adiabatic Wall Calculation

FDNS calculations were made for the inviscid, ideal gas and adiabatic wall conditions in order to compare to the equivalent MOC solutions. The domain of computation was started from the combustor injector faceplate, through the throat, and ended at the nozzle exit plane. Computational results obtained from running the PARC code[18] and RAMP code[2] were also used for comparison. Cases for different specific heat capacity ratios (γ = 1.14, 1.1875, and 1.25) were performed. Figure 1 shows the comparison of vector and Mach number contour for FDNS and PARC solutions at γ = 1.1875. The vectors and Mach numbers show a transition from subsonic flow in the main combustor to sonic flow at the throat, and to supersonic flow in the nozzle. While FDNS is a pressure-based method, PARC is a density-based procedure. Both codes have captured the nozzle shock stemming downstream from the throat, and exhibited similar Mach number contours throughout the computational domain. A sonic line can be observed near the throat region. The computations were made on the same grid with a grid size of 111 × 65.

Figures 2 and 3 show the comparison of centerline and wall pressure distributions for γ = 1.1875 and γ = 1.25, respectively. The FDNS predictions compare well with those of the MOC and PARC results. The sonic start lines obtained from FDNS calculations were used for MOC calculations. The computational time for a typical FDNS ideal gas calculation was estimated as 1.03E-4 CPU s/grid/step on a NASA/MSFC CRAY-XMP. Five hundred iterations were required for near convergence.

Performance calculations of the present method gave specific impulses (ISP) of 426.6, 452.5, and 472.3 for γ = 1.25, 1.1875, and 1.14, respectively. Real gas calculations indicated that the heat capacity ratio ranged from 1.14 at the combustor inlet, to about 1.25 at the nozzle exit. The thermodynamic properties of the combusting gases are very important param-

Table 4 Operating parameters

Mixture ratio	6.000
O_2 Inlet temperature, K	90.56
H_2 Inlet temperature, K	20.56
Chamber pressure, psia	2935.7
Chamber temperature, K	3639.0
Geometric area ratio	77.5

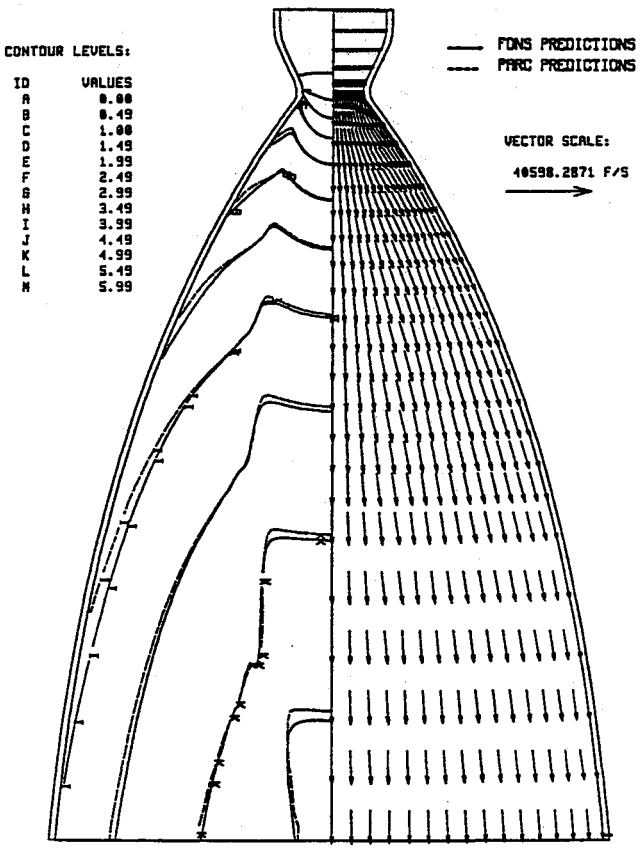

Fig. 1 Velocity vector and Mach number contours for the inviscid, ideal gas (γ = 1.1875), adiabatic wall SSME nozzle flowfield.

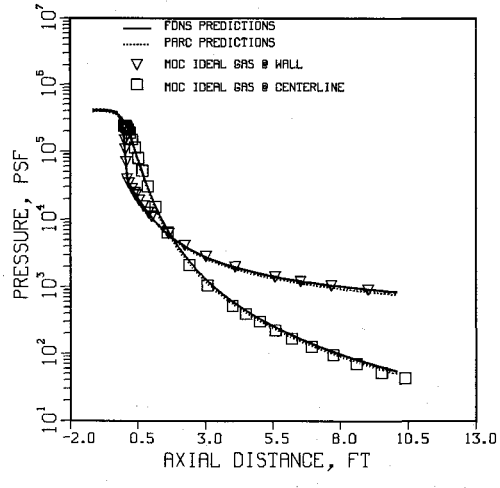

Fig. 2 Comparison of centerline and wall pressure distributions for the inviscid, ideal gas (γ = 1.1875), adiabatic wall SSME nozzle flowfield.

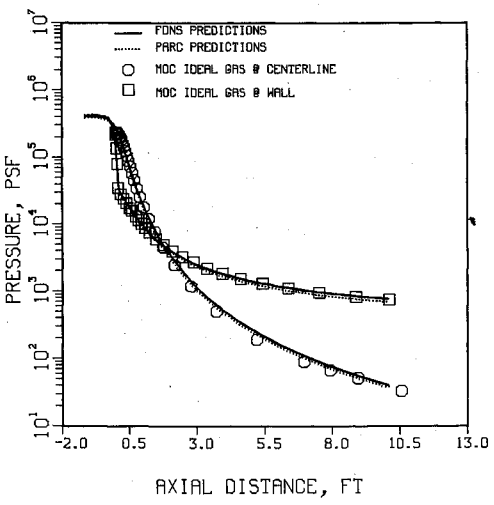

Fig. 3 Comparison of centerline and wall pressure distributions for the inviscid, ideal gas (γ = 1.25), adiabatic wall SSME nozzle flowfield.

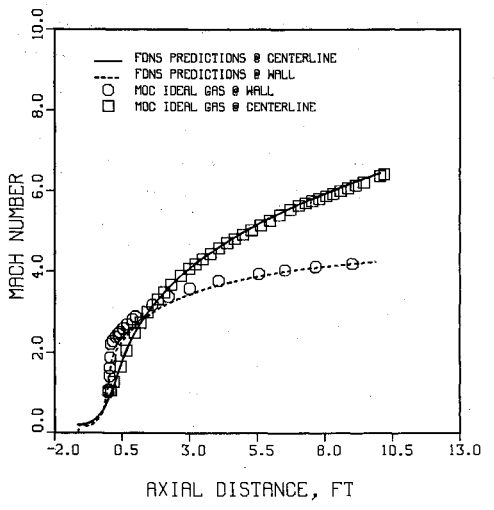

Fig. 4 Comparison of centerline and wall Mach numbers for the inviscid, real gas, adiabatic wall SSME nozzle flowfield.

eters to the accurate prediction of the liquid rocket engine flowfields and performance. A real gas thermodynamics calculation is therefore in order.

Results of the Inviscid, Real Gas, Adiabatic Wall Calculation

The computational domain was extended to include the exhaust plume and the ambient air for the low altitude FDNS real gas calculations. Seven species were considered, including H_2, O_2, H_2O, O, H, OH, and N_2. Chemical equilibrium was assumed to be valid for the entire flowfield. Figure 4 shows the comparison of FDNS and MOC predicted centerline and wall Mach numbers. MOC used an equilibrium properties table obtained from Chemical Equilibrium Calculations (CEC).[17] The FDNS predicted centerline Mach numbers agreed well with those of the MOC predictions. The FDNS prediction of wall Mach number matched the MOC calculation from approximately x = 5.5 ft to the exit plane, but underprediction was revealed near the throat. The underprediction may have been caused by two reasons.

1) A constant perpendicular sonic start line (Mach number = 1.01) was assumed for the MOC calculation that was different from the FDNS calculated sonic line.

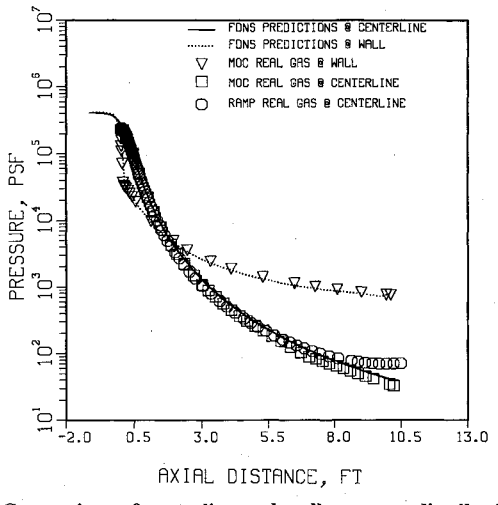

Fig. 5 Comparison of centerline and wall pressure distributions for the inviscid, real gas, adiabatic wall SSME nozzle flowfield.

Table 5 ISP Comparison for inviscid, real gas, and adiabatic wall SSME nozzle

Code	ISP	Chemistry
FDNS	460.4	CHMQGM
MOC	458.4	CEC
TDK	459.2	Finite rate

2) The artificial dissipation used to capture shock by FDNS may have generated excessive total pressure loss, near the starting point of the nozzle shock at the wall.

Nevertheless, the Mach number comparisons for the FDNS and MOC were reasonably good. Figure 5 shows comparisons of the centerline and wall pressure distributions. The FDNS predicted centerline and wall pressure distributions agreed well with those of the MOC predictions. RAMP[2] code overpredicted the centerline pressure slightly near the exit plane.

The FDNS prediction of the SSME nozzle specific impulse is compared to that of MOC and TDK[1] predictions in Table 5. TDK calculation used an eight-reaction finite rate kinetics mechanism. The closeness of all three ISP values indicated that the kinetics loss and shock-kinetics interaction is probably negligible under these circumstances. The computational time for a typical FDNS real gas calculation was estimated to be 2.36E-4 CPU s/grid/step. Approximately 2500 iterations were required for near convergence. The grid size used in this calculation was 201 × 81.

Results of the Viscous, Real Gas, and Cooled Wall Calculation

The simulation of 100% power level SSME fired at sea level, was completed by adding the viscous flow and a specified (measured) wall temperature distribution to the calculation. The extended k-ε turbulence model and wall function approach were used to calculate the viscous flow. Figure 6 shows the comparison of predicted nozzle wall pressure distribution with that of the NASA Marshall Space Flight Center Technology Test Bed (TTB) hot fire test data (test numbers 021, 023, and 025). The three TTB pressure taps were located near the end of the nozzle. The prediction agreed well with the measurement, with a maximum difference of less than one PSI. The error bound for the test data ranged from 10 to 15% for these taps among test firings.

Figure 7 shows the Mach number contour for a calculated conical nozzle flow. The overall features of the nozzle and plume such as nozzle shock, Mach disc, lip shock, plume slip

stream, and Mach disc slip stream were captured quite well. The operating conditions were identical to that of the bell-shaped SSME nozzle as indicated in Table 4, including the nozzle length and the area ratio. This was to see if the proposed method can capture a normal shock for a nearly one-dimensional nozzle flow. From Fig. 7, a nozzle shock formed after the inflection point, hit the centerline, and reflected inside the nozzle; a lip shock formed at the nozzle exit and extended to the triple point in the plume region, where a Mach disc formed beneath the triple point and perpendicular to the axis.

The computed Mach number contour of the bell-shaped SSME nozzle flowfield is shown in Fig. 8. Unlike the nearly one-dimensional conical nozzle flow, a distinctive two-dimensional flow behavior is observed. A slightly curved Mach disc developed in the plume region; the chamber total temperature was recovered behind the Mach disc. The disc location was estimated to be 1.1 nozzle exit radii from the exit plane, with a width of about 1.1 nozzle exit radii. The location and width of the computed normal disc agreed well with those of a hot fire test photograph.[19] Comparisons of the thrust performance of the experimental data, the results of this study, and a TDK/BLM[1] calculated result are shown in Table 6. BLM is a boundary-layer code that provides TDK with the boundary-layer solution. The FDNS calculated ISP value compared very well with that of the experimental data[20] and the TDK/BLM calculation.

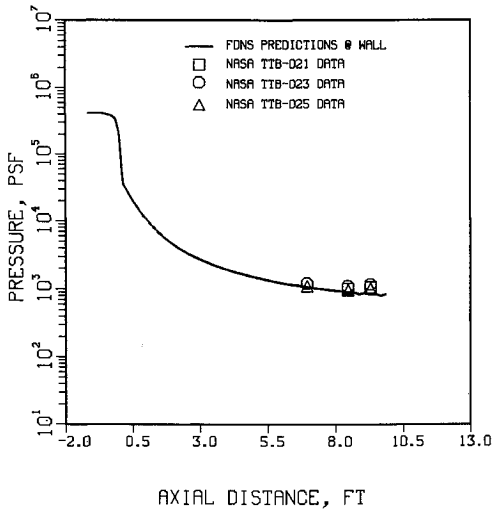

Fig. 6 Comparison of wall pressure distribution for the viscous, real gas, specified wall temperature SSME nozzle flowfield.

The typical grid size used in this calculation was similar to that of the inviscid case, i.e., 201 × 81. The computational time used for one typical run was 2.77E-4 CPU s/grid/step. Approximately 3000 iterations were required for near convergence. The CPU time for a nonreacting case was 2.32E-4 s/grid/step. That means only about 20% increase for an equilibrium chemistry calculation.

Grid Dependency Study

Extensive grid dependency studies were carried out in order to find the best possible computational grids for the liquid rocket engine flowfield and performance calculations. For instance, an inviscid Mach 4 source flow calculation was performed on several grid systems. This grid study was designed to find out general grid clustering strategy for FDNS to preserve total pressure in the absence of a nozzle shock. The velocity vector and pressure contour for the one-dimensional source flow is shown in Fig. 9. A theoretical exit Mach number of 4 and total pressure of 100,000 should be obtained for a grid-independent CFD solution. Table 7 indicates that good solutions can be obtained with grid clustering near the flow inlet.

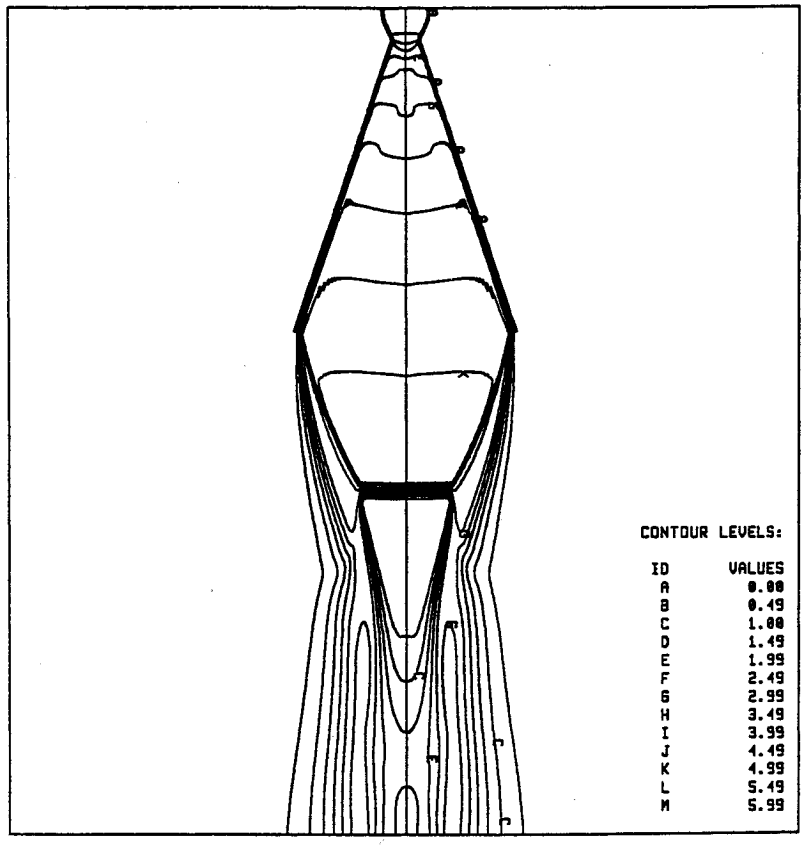

Fig. 7 Mach number contours for a computed conical nozzle flow.

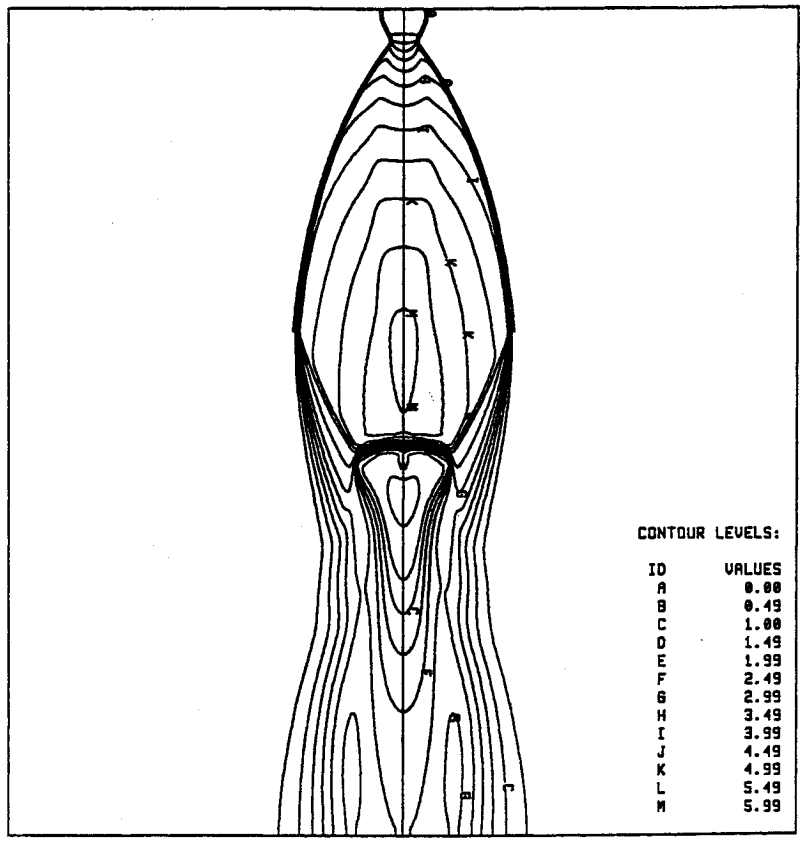

Fig. 8 Mach number contours for a unified SSME combustor, nozzle and plume flowfield.

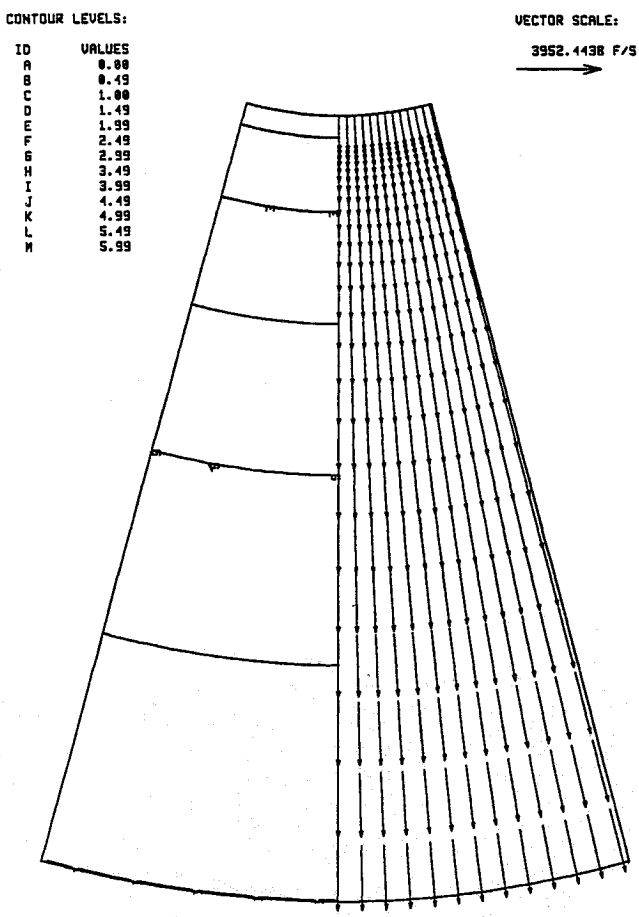

Fig. 9 Velocity vector and Mach number contours for a Mach 4 source flow.

Table 6 ISP Comparison for viscous, real gas, and cooled wall SSME nozzle

	ISP	Chemistry
Experiment	453.3	
FDNS	453.4	CHMQGM
TDK/BLM	452.3	Finite rate

Table 7 Grid study on the inviscid Mach 4 source flow

Run no.	P_{TCE}	P_{TWE}	M_E	Size	Distribution
D41	91,981.4	92,051.2	3.91	50 × 10	Uniform
D45	98,310.0	98,420.0	3.98	100 × 50	Uniform
A46	100,023.0	100,013.0	4.00	100 × 50	Inlet clustered
Theory	100,000.0	100,000.0	4.00		

Conclusions

A pressure-based reactive Navier-Stokes CFD model FDNS has been developed to analyze a unified SSME liquid rocket engine flowfield. The flow domain included the combustion chamber, nozzle, exhaust plume, and the ambient. The code was validated through several systematic stages. For example, the FDNS predicted inviscid nozzle flowfields were compared to those of the MOC, PARC, and RAMP solutions. The comparisons showed that the FDNS predictions were reasonably accurate for inviscid ideal gas and real gas cases. The viscous, real gas, and specified wall temperature case also shows excellent comparison in terms of nozzle wall pressure, Mach disc location, and width to those of the hot fire test. Furthermore, the FDNS predictions of the SSME ISP values were in excellent agreement with those of the MOC and TDK predictions, and the Rocketdyne experimental data. This study demonstrated that the FDNS code predicts the thrust performance and the nozzle/plume flowfield accurately, and it

can be used as a design and analysis tool for general liquid rocket engines.

Acknowledgments

The authors respectfully acknowledge the guidance and support of L. Schutzenhofer and W. Dahm. In addition, the help and suggestions in using MOC codes for code validation from S. Smith, Y. C. Lee, and E. Brewer are also greatly appreciated.

References

[1]Nickerson, G. R., Dang, L. D., and Coats, D. E., "Two-Dimensional Kinetic Reference Program—TDK," Final Rept., Software and Engineering Associates, Carson City, NV, April 1985.

[2]Smith, S. D., "High Altitude Chemically Reacting Gas Particle Mixtures," Vols. I and II for RAMP2, Lockheed Huntsville Research Center, LMSC-HREC TR D867400, Huntsville, AL, Oct. 1984.

[3]Dash, S. M., and Pergament, H. S., "The JANNAF Standard Plume Flowfield Model (SPF)," U.S. Army Missile Command, TR-RD-CR-82-9, Huntsville, AL, April 1981.

[4]Dash, S. M., and Wolf, D. E., "Fully-Coupled Analysis of Jet Mixing Problems, Part I: Shock-Capturing Model, SCIPVIS," NASA CR 3761, Jan. 1984.

[5]Wang, T. S., Chen, Y. S., Farmer, R. C., and Tucker, K., "Numerical Investigation of the Transient SSME Fuel Preburner Combustor Flowfield," AIAA Paper 90-0646, Jan. 1990.

[6]Wang, T. S., Chen, Y. S., and Farmer, R. C., "Numerical Study of Ramjet Dump Combustor Flowfields with a Pressure Based CFD Method," AIAA Paper 89-2798, July 1989.

[7]Sinha, N., York, B. J., Ong, C. C., Stowell, G. M., and Dash, S. M., "3D Navier-Stokes Analysis of High Speed Propulsive Flowfields Using Parch Code," AIAA Paper 89-2796, July 1989.

[8]Kim, S. C., and VanOverbeke, T. J., "Performance and Flow Calculations for a Gaseous H2/O2 Thruster," *Journal of Spacecraft and Rockets*, Vol. 28, No. 4, 1991, pp. 433–438.

[9]Chen, Y. S., and Kim, S. W., "Computation of Turbulent Flows Using an Extended k-ε Turbulence Closure Model," NASA CR-179204, Oct. 1987.

[10]Harten, A., "High Resolution Schemes for Hyperbolic Conservation Laws," *Journal of Computational Physics*, Vol. 49, No. 3, 1983, pp. 357–393.

[11]McCormack, R. W., "Current Status of Numerical Solutions of the Navier-Stokes Equations," AIAA Paper 85-0032, Jan. 1985.

[12]Jameson, A., Schmidt, W., and Turkel, E., "Numerical Solution of the Euler Equations by Finite Volume Methods Using Runge-Kutta Time Stepping Schemes," AIAA Paper 81-1259, June 1981.

[13]Launder, B. E., and Spalding, D. B., "The Numerical Computation of Turbulent Flows," *Computer Methods in Applied Mechanics and Engineering*, Vol. 3, No. 2, 1974, pp. 269–289.

[14]Chen, Y. S., "Viscous Flow Computations Using a Second-Order Upwind Differencing Scheme," AIAA Paper 88-0417, Jan. 1988.

[15]Meintjes, K., and Morgan, A. P., "Performance of Algorithms for Calculating the Equilibrium Composition of a Mixture of Gases," *Journal of Computational Physics*, Vol. 60, No. 2, 1985, pp. 219–234.

[16]David, D., "Space Shuttle Engine Study," Vol. II, Interim Rept., Aerojet Tech. System Co., Sacramento, CA, April 1985.

[17]Svehla, R. A., and McBride, B. J., "FORTRAN IV Computer Program for Calculation of Thermodynamic and Transport Properties of Complex Chemical Systems," NASA TN D-7056, Jan. 1973.

[18]Cooper, G. K., "The PARC Code: Theory and Usage," Sverdrup Technology, Arnold Engineering Development Center, TR-87-24, Arnold AFB, TN, Oct. 1987.

[19]Test No. 901-138, Engine 0005, Negative No. 992105, NASA/MSFC, Sept. 1978.

[20]Neumeyer, R. K., personal communication, SSME Performance and Decision Analysis, Rockwell International, Rocketdyne Div., Canoga Park, CA, Nov. 1989.